High Temperature Corrosion of Materials
https://doi.org/10.1007/s11085-024-10263-w

ORIGINAL PAPER

Decreased Metal Dusting Resistance of Ni-Cu Alloys by Fe and Mn Additions

Anke S. Ulrich[1] · Sergey Kasatikov[2] · Till König[3] · Andrea Fantin[4] · Johannes T. Margraf[5] · Mathias C. Galetz[3]

Received: 12 July 2024 / Revised: 12 July 2024 / Accepted: 17 July 2024

Abstract

Ni-Cu alloys are promising for application at temperatures between 400–900 °C and reducing atmospheres with high C-contents. Typically, under such conditions, metallic materials in contact with the C-rich atmosphere are degraded by a mechanism called metal dusting (MD). Ni-Cu-alloys do not form protective oxide scales, but their resistance is attributed to Cu, which catalytically inhibits the C-deposition on the surface. Adding other alloying elements, such as Mn or Fe, was found to enhance the MD attack of Ni-Cu alloys again. In this study, the effect of the Mn and Fe is divided into two affected areas: the surface and the bulk. The MD attack on binary Ni-Cu alloys, model alloys with Fe and Mn additions, and commercial Monel Alloy 400 is experimentally demonstrated. The surface electronic structure causing the adsorption and dissociation of C-containing molecules is investigated for model alloys. Analytical methods such as scanning electron microscopy combined with energy-dispersive X-ray spectroscopy, electron probe microanalysis combined with wavelength-dispersive X-ray spectroscopy, X-ray diffraction analysis, and near-edge X-ray absorption fine structure measurements were used. The results are correlated to CALPHAD calculations and atomistic simulations combining density functional theory calculations and machine learning. It is found that the Cu content plays a significant role in the surface reaction. The effect of Mn and Fe is mainly attributed to oxide formation. A mechanism explaining the enhanced attack by adding both Fe and Mn is proposed.

Keywords Alloy 400 · Metal dusting · High temperature carburization · High temperature oxidation

Extended author information available on the last page of the article

Published online: 29 July 2024

Introduction

Ni-Cu alloys can be used for applications in reducing high temperature atmospheres with high C-contents. Under such conditions, the structural metallic materials in contact with the C-rich atmosphere are degraded by C-intake into the material. This aggressive form of high temperature corrosion is called metal dusting (MD) corrosion and occurs in the regime of 400 °C–900 °C. Ni-based alloys are usually considered more resistant with increasing concentrations of oxide scale formers. Additionally, alloying with Cu reduces MD attacks. Some of the latest alloys available on the market contain up to 4 wt% of Cu, which is considered to improve the resistance during oxide scale failure. With the increasing demand for more efficient processes, the conditions for structural metallic materials have become more aggressive, causing the need for further alloy development, and considering Cu-rich alloys seems to be a promising route. Previous studies hypothesized that a Cu content of at least 20 wt% in binary Ni-Cu alloys leads to complete inhibition of MD attack [1–4]. This was recently disproved in experiments on binary Ni-Cu alloys with 50 wt% Cu [5]. Additionally, low amounts of Fe and Mn additions to the alloy increased the MD attack tremendously [5]. In commercial Monel Alloy 400 additions of Fe and Mn in combination with C are used to form strengthening carbides [6]. However, Fe and Mn seem to influence MD resistance even without carbide formation, which this work studies.

The MD mechanism for Ni-based alloys is divided into four steps: (i) The initial step is the adsorption and catalytic dissociation of C-containing molecules leading to adsorbed carbon (C*) from the gas phase onto the metal surface. (ii) The incorporation of C from the surface into the material by bulk diffusion and along defects. (iii) Incorporated C causes carbide formation, C accumulation, and graphite crystallization, typically at defects in the material. (iv) The volume expansion due to graphite or carbide formation induces significant stresses, resulting in the internal decomposition of the metallic material. It needs to be clarified on which step minor alloying element additions interact and are potentially detrimental. The addition of Mn and Fe is investigated concerning the change in surface electronic structure influencing catalytic dissociation of C-bearing molecules and their oxide-carbide stabilities inside the reaction zone. Experimental observations and analytical measurements are combined with machine learning (ML) and density functional theory (DFT), aiming at the fundamental understanding of observations in complex atmosphere exposures.

Materials and Methods

Metal Dusting Experiments

The alloys exposed to MD atmosphere are Monel Alloy 400, a Monel Alloy 400 composition without Mn addition, a binary Ni70Cu30 alloy with nominally 70 wt% Ni and 30 wt% Cu, and a Ni69Cu30Mn1 alloy with around 1 wt% Mn addition. The samples were manufactured by additive manufactured using laser powder bed fusion (LPBF). The powder used is produced by gas atomization; for LPBF, an EOS M290 machine equipped with a green laser is used. The laser power was set to 150 W, the hatching distance to 100 µm, and the feed rate to 800 mm/s. The samples were provided by RWTH Aachen and Hochschule Osnabrück. Further details on the manufacturing process can be found elsewhere [5]. Before the MD exposure, the sample surfaces were ground to P1200 grit and cleaned in an ultrasonic bath using ethanol. Sample sizes were measured, and the surface areas were determined.

Two samples of each composition were exposed at $1.8 \cdot 10^6$ Pa and 550 °C to a gas composition of 20%-CO-20%H_2-8%CO_2-1%H_2O-51%Ar. The samples were positioned in Al_2O_3 crucibles to separate the specimens during the exposure. The MD test setup consists of a tube furnace (Carbolite TZF-12/100/900/E301) equipped with a Centralloy ET 45 Micro tube and an inlet Al_2O_3 tube. The furnace was purged with argon for several hours at room temperature. It was subsequently heated up to 550 °C with a heating rate of 10 K/min before starting the exposure to the reducing atmosphere. At process temperature, the gas composition of 20%CO-20%H_2-8%CO_2-1%H_2O-51%Ar was adjusted, and the system was pressurized to $1.8 \cdot 10^6$ Pa. The exposure was conducted in cycles of 240 h. The mass change during exposure was monitored. After 240 h, the furnace was cooled with no defined rate in Ar atmosphere; the samples were cleaned for 10 min in deionized water and 10 min in ethanol using an ultrasonic bath and dried subsequently. Before and after the exposure experiment and after each cycle, macro images of the samples were made. The samples were weighed using a precision weighing balance (Mettler Toledo XP205) with a resolution of 0.05 mg.

After exposure, the samples were half-sectioned parallel to their building direction. They were Ni-plated, mounted in epoxy resin, and ground with SiC papers and diamond suspension to a final surface finish of 1 µm. The cross sections were used to investigate the corrosion products, the subsurface zone, and the sample microstructures using optical microscopy and electron probe microanalysis EPMA (Jeol JXA-8100) equipped with a wavelength-dispersive spectrometer WDS. Alloy compositions were quantitatively determined using 121 point measurements.

Investigation of Electronic Structure

For systematically investigating the surface electronic structure, binary Ni-Cu alloys with Cu concentrations between 5 – 50 wt% were fabricated using electric arc melting. Starting from Ni70Cu30 (wt%), 2 wt% Fe or Mn was added. All

ingots were heat treated for 30 min at 825 °C and 30 min at 600 °C in air based on the heat treatment conventionally used for Monel Alloy 400. Samples of the size $8 \times 8 \times 2$ mm^3 were cut from each ingot after heat treatment. The sample composition was measured using a scanning electron microscope SEM (1540 EsB Cross Beam, Carl Zeiss AG) equipped with an energy-dispersive spectrometer EDS (UltraDry 30 mm^2 Detector; Thermo Fisher Scientific Inc.). Maps with a magnification of around $1000\times$ and lower were analyzed concerning the alloy composition and homogeneity. Back-scattering electron (BSE) and secondary electron images, qualitative element maps, and quantitative element concentrations were measured in a 1×1 mm^2 area. X-ray diffraction XRD (Bruker D8 Advance) equipped with Cu K_α-radiation was conducted using θ-2θ-mode, 0.5 s measuring time, and 0.02° step size.

Near-edge X-ray absorption fine structure (NEXAFS) spectroscopy measurements of the Ni-Cu alloys fabricated by arc melting were performed at the German-Eastern European Laboratory for Energy and Materials Research Dipole (GELEM) at the synchrotron light source BESSY II of Helmholtz-Zentrum Berlin. The NEXAFS spectra were measured at an incident photon angle of 55° with an energy resolution better than $E/\Delta E = 2000$. They were obtained in the total electron yield acquisition mode by measuring drain current. Synchrotron ring current and incident photon flux were used for spectra normalization, with the latter obtained by measuring a gold single-crystal reference.

Density Functional Theory and Machine Learning Method

The reaction step of adsorbing C from the gas phase onto the metal surface is investigated by atomistic simulations. To this end, DFT calculations combined with the MACE-MP-0 ML model were used. The former represents a rigorous first principles electronic structure method [7]. At the same time, the latter was used for fast geometry optimizations and to obtain better statistics regarding the diversity of active sites on alloy surfaces and surface coverages. Five independent simulations were performed for different surface models and coverages for each alloy. The determined energies are averages over these five simulations. To validate the ML model, differential adsorption energies were recomputed for Cu, Ni70Cu30Mn2, and Ni70Cu30Fe2 with single point DFT calculations (using the FHI-aims code [8], PBE functional [9], and 'light' basis set and integration settings). This confirms that the relative coverage dependence for each alloy is well described, with some discrepancies for coverages beyond 50%, where the ML model underestimates adsorbate repulsion somewhat.

The Boudouard reaction was used as a reference, to define the adsorption energy of a C-atom at the surface:

$$E_{ads} = \left[E(C@s) + E\left(CO_{2(g)}\right)\right] - \left[2E\left(CO_{(g)}\right) + E(s)\right]$$

The metal atoms in all alloys are assumed to be randomly mixed. To a first approximation, it was assumed that all C-atoms adsorb at the most stable *fcc* sites on the surface. In principle, both of these assumptions are not entirely valid in the natural system, since certain elements may enrich at the surface and C-atoms can

Table 1 Chemical composition of the investigated Ni-Cu alloys manufactured by LPBF was measured using EPMA/WDS

Alloy name	Ni in wt%	Cu in wt%	C in wt%	Mn in wt%	Fe in wt%	Si in wt%	O in wt%
Monel Alloy 400	67.12 ± 0.35	31.04 ± 0.20	0.51 ± 0.14	1.07 ± 0.03	2.13 ± 0.06	0.22 ± 0.02	0.09 ± 0.05
Monel without Mn	69.49 ± 0.32	29.49 ± 0.22	0.40 ± 0.07	–	2.36 ± 0.05	0.26 ± 0.02	0.10 ± 0.03
Ni69Cu30Mn1	71.28 ± 0.45	29.98 ± 0.25	0.64 ± 0.34	0.97 ± 0.04	–	–	0.05 ± 0.04
Ni70Cu30	71.79 ± 0.35	29.59 ± 0.22	0.42 ± 0.05	–	–	–	0.09 ± 0.04

cluster or diffuse into the metal. Nonetheless, studying adsorption under these well-controlled conditions allows concluding how the composition affects the intrinsic C binding affinity of the alloys, particularly in the low coverage regime.

The surfaces are modeled as 6×6 surface cells so that, in principle, there are 36 *fcc* sites per cell. The coverage $\theta = n/36$, with the number of adsorbates per simulation cell n. To simulate different coverages of the surface, a greedy algorithm is used. Precisely, adsorption energies for all 36 binding sites are first calculated, and the most stable site is chosen for the first adsorbate. Subsequently, the remaining 35 sites are tested for the next C* and the most stable site is selected again. This approach allows the efficient construction of low energy adsorbate configurations, without sampling the complete phase-space for each coverage.

Thermodynamic Calculations

Thermodynamic calculations were conducted to calculate Mn and Fe oxide and carbide stabilities. For these calculations, the CALPHAD method was used to refer to thermodynamic equilibrium. FactSage Software 8.1 was used utilizing the FactPS and customized 8099 databases (GTT-Technologies).

Results and Discussion

Change in MD Resistance by Minor Modifications in Alloy Composition

In Table 1, the compositions of the additively manufactured samples after exposure are shown. The measurements for light elements such as O and C are susceptible to errors using EPMA. However, no significant differences in C and O content were detected, even though Monel Alloy 400 and Monel without Mn have C in their alloy composition.

In Fig. 1 the mass change over exposure time is shown. Monel Alloy 400 shows a much higher mass gain and, therefore, lower resistance to MD compared to the other investigated alloys. Based on the mass change, the macroscopic appearance, and the microscopic investigations of the cross sections after exposure, the resistance to the investigated MD exposure could be ranked with Cu70Ni30 > Monel

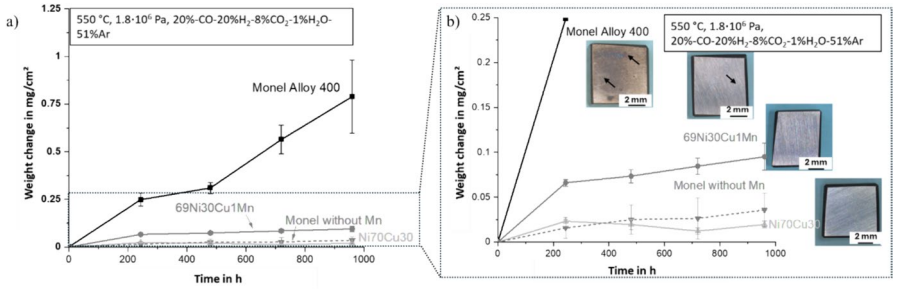

Fig. 1 **a, b** The mass gain per surface area of all investigated alloys over exposure is shown. In **b** macroscopic images after 960 h of exposure are added close to the corresponding mass change curves. The arrows mark a local attack by MD

without Mn > Ni69Cu30Mn1 > > Monel Alloy 400. Concerning the Fe and Mn concentrations listed in Table 1, the resistance can be ranked with 0Fe0Mn > 2Fe0Mn > 0Fe1Mn > > 2Fe1Mn (numbers refer to wt%). The slightly higher resistance seen by the lower mass change of Ni70Cu30 alloy in comparison to Monel without Mn after 960 h of exposure is significant and not attributed to measurement deviations since it is in agreement with other exposures (not yet published) for longer exposure times and in more aggressive atmospheres. Hence, Mn addition has a more detrimental effect on MD resistance than Fe addition, while both elements lead to even worse behavior in combination; the increased MD attack can thus be attributed to Mn and Fe additions.

The reaction zone is exemplified for the Monel Alloy 400 after exposure in Fig. 2. Two areas can be distinguished: Area 1 consists of a layered structure with alternating C-rich layers and metallic alloy remains. A slight O enrichment is detected at the outermost surface overlapping with an enhanced Ni signal in this area. In area 2, the C ingress into the material is less deep and the attack appears more globular than in layers. EPMA elemental distribution maps of Cu, Mn, and

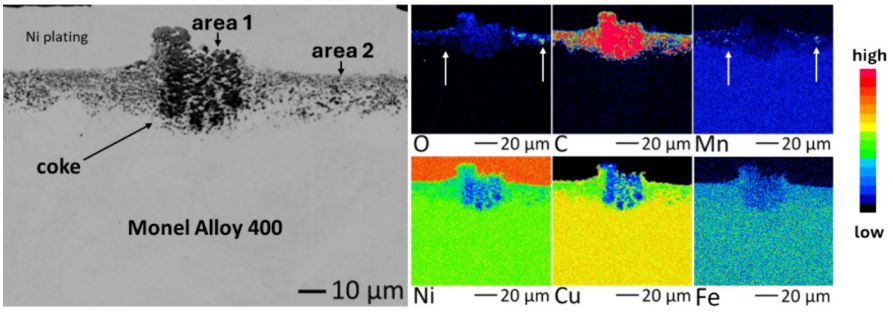

Fig. 2 Cross section of Monel Alloy 400 after 1440 h exposure in 20%-CO-20%H_2-8%CO_2-1%H_2O-51%Ar under $1.8 \cdot 10^6$ Pa pressure, at 550 °C. A BSE image and corresponding elemental distribution maps are shown. The surface is attacked by MD, which is demonstrated by the C-ingress in the material. Overlaps of O and Mn are marked with white arrows in the element maps

Table 2 Chemical composition of the investigated Ni-Cu alloys manufactured by arc melting using SEM/EDS and lattice constants

Alloy name	Ni in wt%	Cu in wt%	Mn in wt%	Fe in wt%	Lattice constant in pm
Ni95Cu5	94.02 ± 0.13	5.36 ± 0.06	–	–	352.9 ± 0.1
Ni80Cu20	78.48 ± 0.11	20.15 ± 0.06	–	–	354.3 ± 0.1
Ni70Cu30	69.99 ± 0.10	28.72 ± 0.07	–	–	355.1 ± 0.1
Ni50Cu50	51.32 ± 0.1	48.55 ± 0.12	–	–	356.9 ± 0.1
Ni68Cu30Mn2	67.72 ± 0.14	30.07 ± 0.09	2.17 ± 0.02	–	355.3 ± 0.1
Ni70Cu28Fe2	69.60 ± 0.11	28.00 ± 0.09	–	2.39 ± 0.02	355.0 ± 0.1

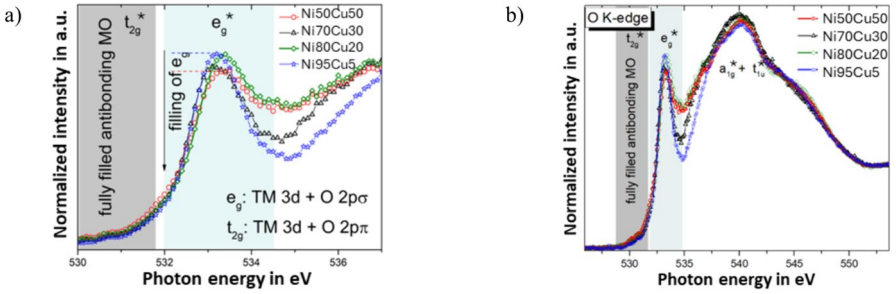

Fig. 3 NEXAFS O K-edge spectra of the binary alloys. The marked regions correspond to electron transitions from the O 1s core level to the unoccupied states of the antibonding MOs (t_{2g}^* and e_g^*), which are characteristic for octahedral TM complexes

O are added and prove an overlap of O and Mn in the reaction zone. Therefore, oxides exist in the reaction zone. Hardly any attack is found for the alloys whose cross sections are not shown here. For Monel without Mn, a slight O enrichment is found at the surface, while for the other samples no changes in surface composition could be detected concerning the used method (EPMA).

Change in Electronic Structure of the Natural Surface Oxide

In Table 2, the alloys and their chemical compositions are listed. All alloys develop a single-phase *fcc* microstructure.

It is well known that the chemisorption of oxygen, surface, and subsurface oxides influence Cu and Ni catalyst performance. Transition metal oxides (TMOs) themselves are widely used for catalytic purposes. The investigations were conducted on metallic surfaces that were exposed to ambient air at room temperature. This is comparable to the initial surface state of the samples exposed to MD conditions before the samples are placed in the furnace.

Figure 3 presents NEXAFS spectra obtained in the vicinity of the O K-edge from the studied binary alloys. The spectra originate from O 1 s core electron excitation to empty 2p states [10]. The overall pattern of the spectra correspond to a fingerprint of amorphous NiO [11, 12]. The local atomic structure of the oxide is universally

represented by Ni^{2+} cations coordinated by 6 O^{2-} anions in octahedral symmetry[10]. Based on the concept of molecular orbitals (MO) and ligand field theory, the first sharp feature of the O K-edge spectra (~533 eV) can be identified as a signal originating from electron transition to empty electron states of an antibonding (marked by *) MO, e_g*. The second broad peak (~540 eV) corresponds to a mixture of empty states belonging to a_{1g}* and t_{1u}* MOs formed by the interaction of Ni 4 s and Ni 4p with O 2p orbitals, respectively. t_{2g}* formed by mixing O 2pπ and Ni 3d orbitals is obscured in the spectra as the corresponding electron states are filled, making the electron transition to these states impossible. Owing to the O_h symmetry, which defines the MO energy order, the t_{2g}* orbital is energetically lower than e_g* (marked in Fig. 3). It is concluded that with increasing Cu content, the electron states of e_g* of the surface oxide become more occupied as the peak is losing intensity (Fig. 3 a)). The most significant change happens in the 20 – 30 wt% range of Cu.

The addition of Fe to Ni70Cu30 depletes t2g*, and the corresponding pre-edge peak emerges, which happens to be fully occupied in the Ni-Cu alloys (see Fig. 4a)). The addition of Mn has a much less pronounced but comparable effect. Although the addition of Fe and Mn have similar effects on the t_{2g}* states, in the Fe case, there are extra changes associated with e_g*. The corresponding O K-edge peak decreases its intensity in Ni70Cu28Fe2, which can be interpreted as filling of the e_g* empty states. Besides, there is a notable intensity rise between of the e_g* peak and the broad second maximum, which might imply the contribution of an additional component emerging within the 534 – 535 eV interval (Fig. 4b)). Such spectral transformations may be induced by the presence of distorted octahedra or even pyramidal coordination (C_{4v} symmetry) resulting in removing of e_g* states degeneracy and splitting of the energy levels [12]. Overall, Fe seems to have a stronger effect on the change in electronic surface structure than Mn.

For additions of Fe, the depletion of the antibonding states correlates well with the increased MD attack. This could also be argued for Mn's slight increase in the depletion of antibonding states. As a tentative assumption, the effect of Mn and Fe can be attributed to a potential increase in the density of unsaturated metal cations (M_{cus}) at the surface. According to a previously suggested model of TMOs surface

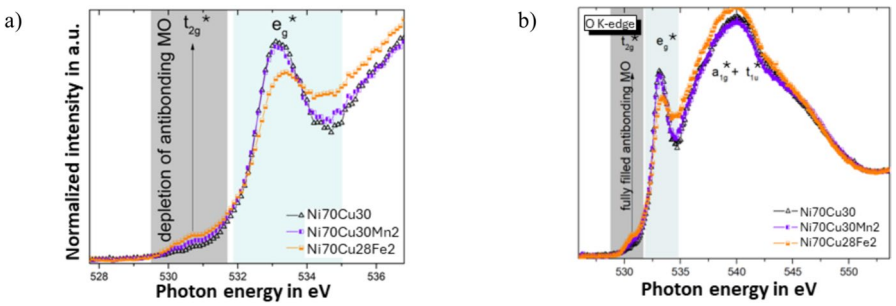

Fig. 4 NEXAFS O K-edge spectra of the studied pristine alloys. The marked regions correspond to electron transitions from the O 1s core level to the unoccupied states of the antibonding MOs (t_{2g}* and e_g*). In **b** a_{1g}* and t_{1u}* are shown

reactivity [13], a higher concentration of M_{cus} at the surface results in more unpaired 3d electrons and overall depletion of antibonding MO states, which correlates with the conclusion derived from the O K-edge spectra of the Fe and Mn containing alloys. The model also states a strong direct correlation between TMOs surface reactivity and M_{cus} density: M_{cus} often behaves as absorption sites. However, the stronger effect of Mn over Fe on MD attack is yet to be explained.

Adsorption Energies and Coverages via Atomistic Simulations

As shown in Fig. 5, a multitude of binding sites can occur on an alloy surface, due to the statistical distribution of the elements. To quantify the stability of adsorbate layers on different alloys as a function of the surface coverage, the differential adsorption energy E_{ads}^{diff} is plotted, which corresponds to the adsorption energy of the last atom added to a slab at a given coverage. The ML-computed curves have been rescaled to reproduce the DFT adsorption energies in the low coverage limit and to capture the reactivity differences between Ni and Cu quantitatively. For the simulations, the bulk composition in contact with the gas atmosphere is considered not including the formation of surface oxides. For the pure metals Cu and Ni, this leads to a step-like dependence between θ and E_{ads}^{diff}. This is because the C atoms initially adsorb onto maximally distant sites. Once occupied, C atoms bind into the gaps between the existing adsorbates. Due to substantial adsorbate–adsorbate repulsion at shorter distances, E_{ads}^{diff} rises markedly every time new types of sites are occupied. As expected, Ni is much more reactive than Cu, with adsorption on the latter being endothermic even at low coverages. By increasing the Cu content of the alloy, the adsorption energy increases; hence, adsorption is less favored. This is more pronounced in the range of Ni95Cu5 to Ni80Cu20, which is in agreement with experimental findings where increased Cu-concentration in Ni decreases MD attack [2, 4]. In addition to adsorbate–adsorbate repulsion, for alloys, the chemical nature of the binding sites plays an important role for the binding strength. Therefore, the order of atom adsorption is such that the most reactive sites with three-fold Ni coordination are occupied first, and the least

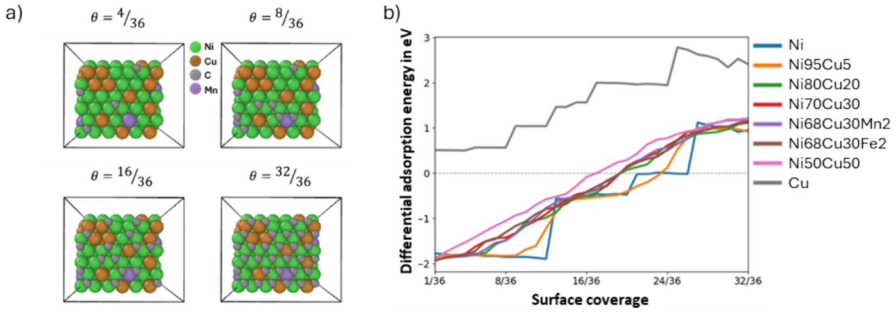

Fig. 5 **a** Exemplary adsorbate configurations for a 6×6 (111) surface cell of Ni68Cu30Mn2 at different coverage states. **b** Differential adsorption energy as a function of surface coverage for Cu, Ni, and different alloys, normalized for Cu(111)

reactive Cu sites are occupied last. This leads to an approximately linear relation between θ and E_{ads}^{diff}. The exception is the Ni95Cu5 alloy, which shows very similar behavior to pure Ni, likely due to the low concentration of Cu sites on the surface. Interestingly, the three alloys Ni70Cu30, Ni68Cu30Mn2, and Ni68Cu30Fe2 show almost identical behavior, in contrast to the NEXAFS findings, which have a probing depth of 10 nm. The influence of Mn and Fe on the enhanced MD attack, therefore, cannot be attributed to differences in C surface adsorption, which may be related to the properties of the corresponding surface oxides.

Thermodynamic Stabilities

The thermodynamic stabilities of Fe- and Mn oxides and carbides are shown in Fig. 6.

In addition, the C-activity a_c of the MD gas used in the conducted experiments and calculated after [14] and the oxygen partial pressure $p(O_2)$ of the MD gas are marked. Concerning the used conditions, MnO is stable in case of Mn alloying at 550 °C and Fe_3O_4 is stable in case of Fe alloying. The phase boundaries are not influenced by combination, as shown in Fig. 6c). Under the considered equilibrium conditions, Ni and Cu are stable in their elemental state. At the beginning of the exposure, as the gas is switched from Ar (~2 ppm O_2) to the test atmosphere by reaching 550 °C, $p(O_2)$ decreases while the a_c rises. It is assumed that the Ni oxide observed on the surface by NEXAFS is reduced, while Mn and Fe oxides remain. Fe_3O_4 and MnO are stable at the material surface under the investigated experimental conditions. By covering the surface with adsorbed molecules or dissociated C, the oxygen $p(O_2)$ decreases. Below around $0.5 \cdot 10^{-31}$ Pa, Fe_3O_4 is reduced and Fe_3C is stable. On the contrary, MnO is stable until $p(O_2)$ drops below $0.5 \cdot 10^{-43}$ Pa which agrees with the experimental findings of overlapping Mn and O signals.

Effects of Alloying Elements on Metal Dusting Mechanism

Two affected areas can be defined: the surface and the bulk. Considering the surface first and, therefore, the metal-gas interaction, the main C-source in this study is provided by $CO_{(g)}$ via Boudouard and syngas reaction. Thus, $CO_{(g)}$ is used for the schematic drawing in Fig. 7a. The findings in this study that Cu decreases MD attack by a decrease in catalytic surface activity confirm the previously proposed

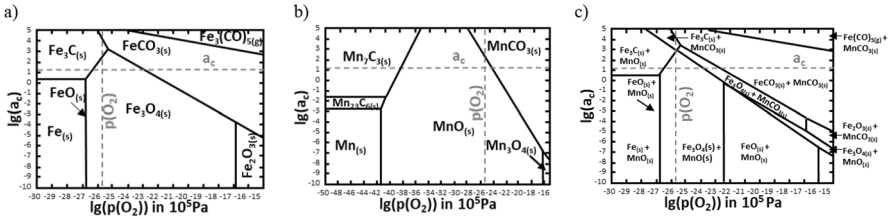

Fig. 6 Thermodynamic stabilities of **a** Fe–O-C, **b** Mn–O-C, and **c** Mn-Fe–O-C at 550 °C and $1.8 \cdot 10^6$ Pa in 20%-CO-20%H_2-8%CO_2-1%H_2O-51%Ar

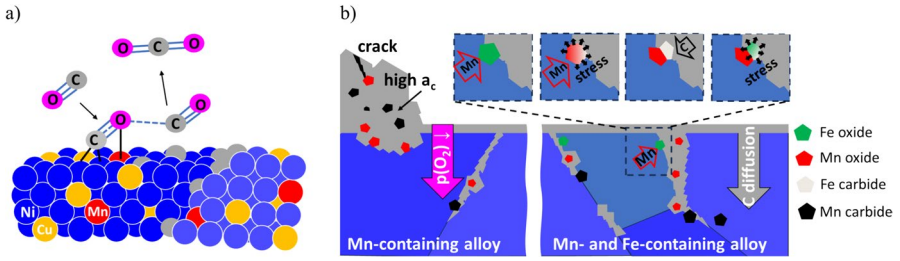

Fig. 7 **a** Schematic drawing of the interplay between CO and the metallic surface. The C-atom interacts with the electronic surface states of Ni, while the O-atom interacts with an oxide forming element. **b** Proposed mechanism enhancing MD attack for Mn- and Fe additions to Ni-Cu alloys. The interplay of oxide and carbide formation is visualized

effect of Cu [15]. However, the previously proposed threshold of around 20 wt% is not confirmed even though the effect of increasing Cu addition to Ni on the inhibition of MD decreases up from either 20 – 30 wt% (NEXAFS) or ~ 5 – 20 wt% (atomistic simulations). The difference between both might arise as the investigations refer to different scales and the formation of native oxides was not considered in the atomistic simulations. The initial state of the surface, e.g., native oxides such as Ni oxide or metallic alloying elements, play a role in the beginning of exposure as they change the surface states and enhance adsorption. The dissociation of $CO_{(g)}$ or other C-containing molecules is enhanced by weakening the CO bond. This happens by enhancing the interaction of the C-atoms or the O-atom's interaction with the surface. Fe was found to have a stronger effect on the change in electronic surface states compared to Mn (see Fig. 4). From investigations on catalysts for oxygen evolution reaction, it is known that TM oxides (e.g., the native oxides) enhance the surface bonding strength of O-atoms [13]. Additionally, TM oxides are known to interact with C during catalytic reactions or carbo nanotube formation. Besides the native oxide scales, the same effect on the weakening of the CO bond by coupling with the O-atom orbitals is also true for pure metallic elements like Mn or Fe. In contrast, the atomistic simulations show that metallic Mn or Fe does not influence the adsorption of the C-atom. The oxidation of Mn to MnO, which is stable under the investigated experimental conditions (compare Fig. 6), is more favored than the oxidation of Fe to Fe_3O_4 by $CO_{(g)}$, considering the involved reaction partners. The change in surface electronic structure and number of reactants for oxidation of Mn and Fe influences the MD attack at the beginning of the exposure at the surface. Still, it does not explain why combining Fe and Mn additions enhances the MD attack dramatically.

For analyzing the effect of Mn and Fe on the MD attack taking place in the bulk (steps (ii) – (iv) mentioned in the introduction), it is assumed that due to the fabrication process using LPBF, the defect densities in the samples (e.g., grain sizes, dislocations, internal carbides) are high and comparable. The differences in performance are, therefore, related to the compositional deviations. For the binary alloys, the dissolved C-concentration is assumed to decrease with increasing Cu content as Cu has a much lower solubility limit (e. g. at 900 °C, Cu: 0.016 at.% C, Ni: ~ 1 at.% [16, 17]). Hence, less C can nucleate at defects and

form graphite or carbides causing material degradation. As shown in Fig. 2 and reported in an earlier study [5], the main difference between Fe and Mn additions is the formation of Mn oxides in the reaction zone under the investigated conditions, while overlaps of Fe and O were not detected. Even though Fe_2O_3 is thermodynamically stable under the experimental conditions (see Fig. 6a)), Fe_2O_3 forms at or close to the surface due to its lower stability than MnO. MnO is stable at lower $p(O_2)$. Therefore, it is found deeper in the material. Mn oxides or carbides form preferentially at grain boundaries or defects depending on the local $p(O_2)$ and a_c (schematically shown in Fig. 7b)). Internal oxide and carbide formation induces stresses. In the case of cracking, $p(O_2)$ increases locally. If carbide formation is considered, an oxidation of those is possible and C is rereleased. Mn has a much more detrimental effect than Fe because its carbides and oxides are more stable and form deeper in the material. Depending on the local $p(O_2)$ and a_c, an additional effect is the existence of two Mn carbides, which can cause additional stresses due to phase transformation. Comparing areas 1 and 2 in Fig. 2, oxides are not present in the region of highest attack. A possible explanation is that with increasing ac in the oxide vicinity by C-incorporation or if the material is buried under reaction products, the oxides are reduced by forming gaseous species such as $CO_{2(g)}$ and $CO_{(g)}$, which release degrades the reaction zone (compare Fig. 7b) left).

Combining both element additions, Mn and Fe, as it is the case in Monel Alloy 400, the overall concentration of alloying elements (Fe + Mn = 3 wt%) is higher, but this alone cannot explain the much higher MD attack. As the stability of MnO is higher, it preferentially forms an oxide, which might enhance the carburization of Fe. However, in the case of Fe_3O_4 formation, a reduction by Mn is possible. Mn is known to be a fast-diffusing element, e.g., Mn bulk diffusion in Ni is with a diffusion coefficient $D = 1.3 \cdot 10^{-21}$ m^2/s more than two orders of magnitude higher compared to Fe bulk diffusion in Ni ($D = 6.8 \cdot 10^{-23}$ m^2/s) at 550 °C [17,18]. Due to the polycrystalline nature of the LPBF material and the high defect density, the diffusion of all elements is assumed to be much faster via short-circuit diffusion paths. Hence, an interplay between oxidation and carburization in between Fe- and Mn species is considered the origin of the enhanced MD attack by combining Mn and Fe. Further investigations are needed to elaborate further on this theory.

Acknowledgements The financial support by AIF (IGF Nr. 20904 N) and DFG (UL 591/1-1) is gratefully acknowledged. The Helmholtz-Zentrum Berlin is thanked for granting measurements at the synchrotron BESSY II (232-12521-EF). Andrea Fantin acknowledges DFG for funding (FA1817/1-2). Dr. Gerald Schmidt, DECHEMA Research Institute, for EPMA measurements, is gratefully acknowledged. The authors thank Prof. Dr.-Ing. Ulrich Krupp, RWTH Aachen, Prof. Dr.-Ing. Katrin Jahns, Hochschule Osnabrück, and Lukas Reiff, RWTH Aachen, for providing the LPBF material.

Author Contribution Atomistic simulations were done by J.M. Funding acquisition was done by A.F., A.U., and M.G. Investigations were done by A.F., A.U., S.K., and T.K. Project administration was done by A.U. Resources were done by A.F., A.U., J.M., and M.G. Writing—original draft was done by A.U., J.M., and S.K. Writing—review and editing was done by all authors. Visualization was done by A.U., J.M., S.K., and T.K.

Funding Open Access funding enabled and organized by Projekt DEAL. AiF Projekt (20904 N), Deutsche Forschungsgemeinschaft, UL 591/1-1 (531328306), FA1817/1-2, Helmholtz-Zentrum Berlin (232-12521-EF).

Data Availability The datasets are available on request.

Declarations

Conflicts of interest The authors declare that they have no known competing financial interests or personal relationships that could have appeared to influence the work reported in this paper.

References

1. J. Zhang, D. M. I. Cole, and D. J. Young, *Materials and Corrosion* **56**, 2005 (756).
2. Y. Nishiyama, K. Moriguchi, N. Otsuka, et al., *Materials and Corroions* **56**, 2005 (806).
3. J. Zhang and D. J. Young, *ECS Transactions* **3**, 2007 (27).
4. C. Chun, S. Desai, and T. A. Ramanarayanan, *Corrosion* **68**, 2012 (810).
5. K. Jahns, A. S. Ulrich, C. Schlereth, et al., *Oxidation of Metals* **96**, 2021 (241).
6. G. K. Dey, R. Tewari, P. Rao, et al., *Metallurgical Transactions A* **24**, 1993 (2709).
7. Batatia I, Benner P, Chiang Y, et al. A foundation model for atomistic materials chemistry. *arXiv preprint* arXiv:2401.00096 *2024.*
8. V. Blum, R. Gehrke, F. Hanke, et al., *Computer Physics Communications* **180**, 2009 (2175).
9. J. P. Perdew, K. Burke, and M. Ernzerhof, *Physics Review Letters* **77**, 1996 (3865).
10. J. G. Chen, *Surface Science Reports* **30**, 1997 (1).
11. Z. Y. Wu, C. M. Liu, L. Guo, et al., *The Journal of Physical Chemistry B* **109**, 2005 (2512).
12. R. Li, S. Yang, Y. Zhang, et al., *Cell Report Physical Science* **3**, 2022 (100788).
13. H. B. Tao, L. Fang, J. Chen, et al., *Journal of the American Chemical Society* **138**, 2016 (9978).
14. C. Schlereth, K. Hack, and M. C. Galetz, *Corrosion Science* **206**, 2022 (110483).
15. D. J. Young, J. Zhang, C. Geers, et al., *Materials and Corrosion* **62**, 2011 (7).
16. M. Singleton and P. Nash, *Bulletin of Alloy Phase Diagrams* **10**, 1989 (121).
17. S. I. Ryabtsev, V. F. Bashev, A. I. Belkin, et al., *The Physics of Metals and Metallography* **102**, 2006 (305).

Authors and Affiliations

Anke S. Ulrich[1] · Sergey Kasatikov[2] · Till König[3] · Andrea Fantin[4] · Johannes T. Margraf[5] · Mathias C. Galetz[3]

✉ Anke S. Ulrich
silvia.ulrich@uni-bayreuth.de

Sergey Kasatikov
sergey.kasatikov@helmholtz-berlin.de

Till König
till.koenig@dechema.de

Andrea Fantin
andrea.fantin@bam.de

Johannes T. Margraf
johannes.margraf@uni-bayreuth.de

Mathias C. Galetz
mathias.galetz@dechema.de

[1] Metals and Alloys II, Faculty of Engineering Science, University of Bayreuth, Prof.-Rüdiger-Bormann-Str. 1, 95447 Bayreuth, Germany

[2] Institute of Applied Materials, Helmholtz-Zentrum Berlin für Materialien und Energie GmbH, 14109 Berlin, Germany

[3] Materials and Corrosion, DECHEMA-Forschungsinstitut, Theodor-Heuss-Allee 25, 60486 Frankfurt, Germany

[4] Department of Materials Engineering, Bundesanstalt für Materialforschung und -prüfung, Unter den Eichen 87, 12205 Berlin, Germany

[5] Bavarian Center for Battery Technology (BayBatt), University of Bayreuth, Weiherstraße 26, 95448 Bayreuth, Germany